Available online at www.sciencedirect.com
SCIENCE DIRECT®
Journal of Solid State Chemistry 178 (2005) 2091–2103
JOURNAL OF SOLID STATE CHEMISTRY
www.elsevier.com/locate/jssc

Ternary rare-earth alumo-silicides—single-crystal growth from Al flux, structural and physical properties

Svilen Bobev[a,*], Paul H. Tobash[a], Veronika Fritsch[b], Joe D. Thompson[b], Michael F. Hundley[b], John L. Sarrao[b], Zachary Fisk[c]

[a]*Department of Chemistry and Biochemistry, University of Delaware, Newark, DE 19716, USA*
[b]*MST-10, Los Alamos National Laboratory, Los Alamos, NM 87545, USA*
[c]*Department of Physics, University of California, Davis, CA 95616, USA*

Received 23 February 2005; received in revised form 15 April 2005; accepted 19 April 2005

Abstract

A number of rare-earth alumo-silicides (*R*-Al-Si) have been synthesized from the corresponding elements by high-temperature reactions, carried out in excess of aluminum to serve as a flux. Under these experimental conditions, large single crystals of all *R*-Al-Si ternary phases were readily produced. The crystal structures these ternaries adopt were studied by means of powder and single-crystal X-ray diffraction and were classified as follows: (1) the early rare-earths (R = La, Ce, Pr, Nd, Sm, Gd) yield RAl_xSi_{2-x}, $x\sim1$, non-stoichiometric ternary derivatives of the body-centered α-$ThSi_2$-type; (2) the late rare-earths (R = Tb, Dy, Ho, Er, Tm) form stoichiometric $R_2Al_3Si_2$ compounds that crystallize in the *C*-centered monoclinic $Y_2Al_3Si_2$-type; (3) the divalent Eu and Yb produce $EuAl_2Si_2$ and $YbAl_2Si_2$ with the trigonal $CaAl_2Si_2$-type, whereas the last lanthanide element, Lu, forms LuAlSi with *C*-centered orthorhombic YAlGe-type. These structural trends are reviewed, and the evolution of the basic physical properties such as magnetism, heat capacity and electrical resistivity when moving across the series is described in detail.

Keywords: Rare-earth intermetallics; Crystal structure; Magnetic measurements; Flux growth

1. Introduction

Binary rare-earth silicides and germanides have been extensively studied during the last several decades [1–3]. The tremendous interest in these scientifically important materials has resulted in numerous papers, review articles, books and monographs, and the number of publications continues to grow. Of particular interest to us is the mixed-valent and Kondo behavior observed in $CeSi_2$ [4]. This compound forms congruently according to the known phase diagram and crystallizes in the body-centered tetragonal α-$ThSi_2$ structure type [3]. However, there is a certain homogeneity region in the Ce-Si system, ranging from approximately 64 to 66.7 at% Si, which presents a significant challenge for obtaining $CeSi_{2-x}$ as a single-phase product with a fixed value of x. Moreover, from the crystal structure, one might expect rather anisotropic physical properties and the availability of sizeable single crystal with known and well-defined composition becomes of crucial importance for unequivocal property measurements.

Thus, motivated by the successful application of the high-temperature flux techniques [5], we decided to explore opportunities to grow single crystals of $CeSi_2$ in a variety of low melting metal fluxes (M), such as Al, Ga, In, Sn, Pb, etc. These experimental efforts, carried out over a period of almost 10 years, proved that this method yields large and nicely faceted single crystals, which, however, formed ternary substituted derivatives with a general formula CeM_xSi_{2-x}. Because of the relatively good solubility of Si in Al and Ga in

*Corresponding author. Fax: +1 302 831 6335.
E-mail address: sbobev@chem.udel.edu (S. Bobev).

0022-4596/$ - see front matter © 2005 Elsevier Inc. All rights reserved.
doi:10.1016/j.jssc.2005.04.021

particular, we find a number of solid solution phases $CeAl_xSi_{2-x}$ and $CeGa_xSi_{2-x}$, in which the physical properties change dramatically with x. It was also observed that certain structure changes occur, most notably from body-centered α-$ThSi_2$-type to hexagonal AlB_2-type as x increases. Further, the value of x depends on reaction conditions—initial stoichiometry, reaction temperature, cooling rates, etc. The lack of good control over these parameters hampered somewhat quick progress along these lines of research.

Recently, several publications on the phase equlibria and properties in the systems R-Al-Si (R = rare-earth metal) appeared [6–9]. Possible homogeneity ranges and associated structure-property relationships in the systems Ce-Al-Si and Ce-Al-Ge have been discussed [6]. This stimulated us to review the data we have gathered over the years and complement the results from these investigations. We have extended the studies on Ce-Si and Ce-Al-Si to cover the whole series of rare-earth metals, and herein we report on the evolution of the crystal structures in the system R-Si under Al flux conditions, going from La to Lu, as well as on the evolution of physical properties when moving across the series. It was found that under these experimental conditions, the early rare-earths (R = La, Ce, Pr, Nd, Sm, Gd) yield RAl_xSi_{2-x}, ternary derivatives of the body-centered α-$ThSi_2$-type, whereas the late rare-earths (R = Tb, Dy, Ho, Er, Tm) form stoichiometric $R_2Al_3Si_2$ compounds that crystallize in the C-centered monoclinic $Y_2Al_3Si_2$-type [10]. The divalent Eu and Yb behave differently, as expected, and were found to produce $EuAl_2Si_2$ and $YbAl_2Si_2$ with the trigonal $CaAl_2Si_2$-type [11], while the last lanthanide element, Lu, forms LuAlSi with C-centered orthorhombic YAlGe-type [12]. A subsequent publication will discuss the same trends in the systems R-Si-Ga and R-Ge-Al/R-Ge-In under flux-growth conditions [13]. Physical property measurements on $EuAl_2Si_2$ and $YbAl_2Si_2$ single crystals will be reported elsewhere relative to the prospect for mixed-valent behavior [13].

2. Experimental

2.1. Synthesis

Single crystals of the title compounds were grown using the high-temperature flux technique using molten Al as a solvent. Rare-earth metals with >99.9% purity from Ames Laboratory were used as received. Al (shot) and Si (lump), both with purity greater than 99.999%, were obtained from Alfa-Aesar. Typically, the reactions were carried out in 5 cm^3 alumina crucibles, which were encapsulated in evacuated fused silica jackets by flame sealing. Different temperature profiles were used, e.g., quick or slow ramping to 1175 °C, homogenization for up to 2 h, cooling to 750, 700 or 675 °C (above the melting point of Al, 660 °C) at various rates. At these temperatures, the molten Al was removed by centrifugation. Further and more elaborate details on the flux-growth synthetic procedures can be found elsewhere [5].

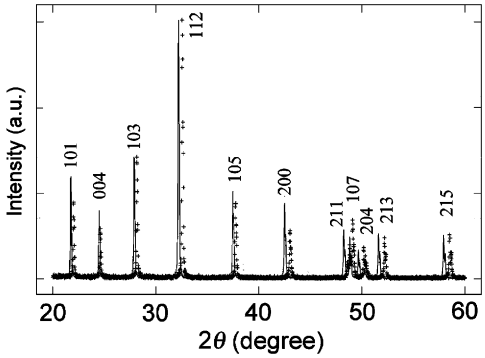

Fig. 1. Powder diffraction data for $CeAl_xSi_{2-x}$. Data (superimposed) for two different reaction batches of $CeAl_xSi_{2-x}$ are shown. Significant shifts in the peak positions are clearly seen reflecting differences in lattice constant. These results confirm the broad stoichiometric breadth for $CeAl_xSi_{2-x}$ (α-$ThSi_2$-type), which according to Ref. [6] spans $0.45 < x < 1.28$. (For the samples for which data are presented, the only difference in the synthetic procedure is the cooling rate.)

In all instances, the reaction products were large single crystals with well-defined crystal morphology. The crystals appear to retain their shiny metallic luster over a period of several years. No other phases besides residual Si and Al were present according to powder X-ray diffraction studies (see below). However, as mentioned already, some variations in the crystal structure and properties were observed when comparing crystals from different reaction batches (Fig. 1). Therefore, all physical property measurements discussed below were carried out on single crystals grown using the same synthetic procedures: atomic ratios R:Si:Al = 1:2:20, ramping rate 200 °C/h, reaction temperature 1175 °C, 2 h dwell, followed by cooling to 700 °C at a rate of −30 °C/h. Aluminum flux was effectively removed by centrifugation at 700 °C and the crystals (plates or needles, depending on the structure type) did not have to be treated with solutions of NaOH in order to remove residual Al. For those R-Al-Si systems in which wide homogeneity ranges were found to exist, e.g., Ce-Al-Si and Pr-Al-Si, the same crystal was used for all physical property measurements, and its exact chemical composition was subsequently determined by means of chemical analysis (below).

2.2. X-ray diffraction studies

X-ray powder diffraction patterns were taken on a Scintag XDS 2000 with monochromated Cu $K\alpha$ radiation (λ = 1.5406 Å). The samples were prepared from

single crystals, which were subsequently crushed and ground to fine powders in agate mortars. The powdered specimens were then placed on rotating sample holders, and powder X-ray diffraction data were routinely collected in continuous scan mode up to a 2θ limit of 80° with an interval of 1.0°/min. The collected X-ray powder diffraction data were used for phase identification, as well as for unit cell parameter determination in order to check for any potential phase width. This was done by a least-squares refinement of the positions of the lines, calibrated by silicon as an internal standard with JADE 6.5 [14] and GSAS software packages [15]. Variations in the resulting lattice parameters for samples with identical starting materials, synthesized under different conditions, were significant in the case of all $R\mathrm{Al}_x\mathrm{Si}_{2-x}$ (R = La, Ce, Pr, Nd) phases, as illustrated in Fig. 1 (Table 1).

To check and unequivocally establish the structure type and to verify the site occupancies for $R\mathrm{Al}_x\mathrm{Si}_{2-x}$ (R = La, Ce, Pr, Nd, Sm, Gd), a single crystal of $\mathrm{GdAl}_x\mathrm{Si}_{2-x}$ was selected and mounted on the top of a glass fiber (silver-metallic, plate-like shape, $0.14 \times 0.08 \times 0.06\,\mathrm{mm}^3$). Intensity data were collected on a Bruker SMART 1000 single-crystal diffractometer with monochromated Mo $K\alpha$ radiation at room temperature (0.3° ω scans, $2\theta_{\max} = 62^\circ$, a full sphere). A total of 502 reflections were collected using the SMART software [17], and were subsequently corrected for Lorentz and polarization effects and integrated with the aid of the SAINT package [18]. Empirical absorption correction was applied based on SADABS [19]. Merging the raw data in Laue symmetry $4/mmm$ confirmed the systematic absence condition $h+k+l \neq 2n$ for the body-centered lattice. The reflection conditions $hk0$ for $h,k = 2n$, and $0kl$ for $k,l = 2n$ were all satisfied; thus, the α-ThSi_2 structure type was adopted as the initial structure model [6]. The structure was refined on F^2 with the aid of SHELXTL V5.10 [20]. The refinements showed no indications that either Gd or Si sites might be partially occupied: when the site occupancies were allowed to vary, no deviations greater than 3σ were observed. Therefore, in the final refinement cycles, all occupation factors were kept at 100% with the Si site modeled as a statistical mixture Si/Al = 50/50. Elemental analysis (below) on crystals from the same reaction batch confirmed the sample composition $\mathrm{GdAl}_{0.98(3)}\mathrm{Si}_{1.02(3)}$. Hence, for the sake of simplicity, it will be referred to as GdAlSi hereafter. Further details of the data collection and structure refinements are given in Table 2, while positional and equivalent isotropic displacement parameters are listed in Table 3.

Low-temperature single-crystal diffraction data were also collected for all $R_2\mathrm{Al}_3\mathrm{Si}_2$ (R = Tb, Dy, Ho, Er, Tm) compounds, aimed to ascertain the robustness of the monoclinic $Y_2\mathrm{Al}_3\mathrm{Si}_2$-type in which these compounds crystallize. Diffraction data were collected at 120 K using the above-mentioned routines. The results agree very well with previous room temperature work on $R_2\mathrm{Al}_3\mathrm{Si}_2$ (R = Tb, Dy) [21], and on $R_2\mathrm{Al}_3\mathrm{Si}_2$ (R = Ho, Er, Tm) [22], and unambiguously confirmed that the latter are compounds with no stoichiometry breadth. The unit cell parameters at 120 K were slightly smaller than those at room temperature yielding volume expansion coefficients (β) in the order of $10^{-5}\,\mathrm{K}^{-1}$, a behavior which is quite typical of metals and intermetallic compounds. Further details of the crystal structure investigations can be obtained from the Fachinformationszentrum Karlsruhe, 76344 Eggenstein-Leopoldshafen, Germany (fax: +49 7247 808 666; e-mail: crysdata@fiz.karlsruhe.de) on quoting the depository numbers: CSD 415151 ($\mathrm{GdAl}_{0.98(3)}\mathrm{Si}_{1.02(3)}$); CSD 415146 ($\mathrm{Tb}_2\mathrm{Al}_3\mathrm{Si}_2$); CSD 415147 ($\mathrm{Dy}_2\mathrm{Al}_3\mathrm{Si}_2$); CSD 415148 ($\mathrm{Ho}_2\mathrm{Al}_3\mathrm{Si}_2$); CSD 415149 ($\mathrm{Er}_2\mathrm{Al}_3\mathrm{Si}_2$); CSD 415150 ($\mathrm{Tm}_2\mathrm{Al}_3\mathrm{Si}_2$).

2.3. Magnetic susceptibility measurements

Field-cooled dc magnetization measurements were performed in a Quantum Design MPMS SQUID magnetometer from 1.8 to 350 K in a magnetic field of 1 kG. Several specimens from different reaction batches were measured in order to provide reproducible results. The samples (single crystals, which were then used for all other measurements, followed by chemical analysis) were secured between pieces of quartz wool and suspended in a low background sample holder. Field-dependent studies on some samples were also performed.

2.4. Resistivity measurements

Electrical resistivity measurements were carried out in a Quantum Design PPMS system using a four-probe technique from 4 to 350 K with excitation currents between 1 and 3 mA. Resistivities were measured on at least two crystals from each batch to assure reproducibility. For all data reported herewith, sand-paper polished single crystals were used to minimize geometric errors. No measurements in field were completed at this time.

2.5. Calorimetry

Specific heat data for some of the R-Al-Si samples were measured in a He^4 cryostat using the thermal relaxation method in the temperature range 1.3–20 K.

2.6. Elemental analysis

Several carefully selected single crystals of $R\mathrm{Al}_x\mathrm{Si}_{2-x}$ (R = La, Ce, Pr, Nd, Sm, Gd) were analyzed with a Cameca SX50 electron microscope equipped with a

Table 1
Ternary compounds in the *R*-Al-Si system (R = La to Lu, excl. Pm)

Compound	Structure	Unit cell parameters[a]					Reference
		a (Å)	b (Å)	*c* (Å)	*β* (deg.)	*V* (Å^3)	
$LaAl_{1.04}Si_{0.96}$	α-$ThSi_2$ ($I4_1/amd$)	4.3102(3)		14.5775(9)		270.82	This work[b]
LaAlSi	—	*4.284*		*14.56*		*267.2*	[16]
$CeAl_{1.02}Si_{0.98}$	α-$ThSi_2$ ($I4_1/amd$)	4.2491(1)		14.5108(4)		261.99	This work[b]
$CeAl_{0.85}Si_{1.15}$	—	4.2030(1)		14.4619(5)		255.47	This work[c]
$CeAl_{1.2}Si_{0.8}$	—	*4.2741(1)*		*14.732(1)*		*269.12*	[6]
CeAlSi	—	*4.242*		*14.538*		*261.60*	[7]
$CeAl_{1.2}Si_{0.8}$	—	*4.280*		*14.755*		*270.29*	[7]
$CeAl_{1.4}Si_{0.6}$	—	*4.280*		*14.90*		272.8	[16]
$PrAl_{1.19}Si_{0.81}$	α-$ThSi_2$ ($I4_1/amd$)	4.2263(1)		14.5343(5)		259.61	This work[b]
$PrAl_{1.15}Si_{0.85}$	—	4.2245(1)		14.4731(5)		258.29	This work[b]
$NdAl_{1.11}Si_{0.89}$	α-$ThSi_2$ ($I4_1/amd$)	4.2030(1)		14.4647(6)		255.52	This work[b]
$SmAl_{1.07}Si_{0.93}$	α-$ThSi_2$ ($I4_1/amd$)	4.1577(1)		14.4098(6)		249.10	This work[b]
$EuAl_2Si_2$	$CaAl_2Si_2$ ($P\bar{3}m1$)	4.180(2)		7.252(4)		109.75	This work
$EuAl_2Si_2$	—	*4.181(1)*		*7.259(1)*		*109.89*	[33]
$GdAl_{0.98}Si_{1.02}$	α-$ThSi_2$ ($I4_1/amd$)	4.1255(1)		14.4259(5)		245.53	This work[b]
GdAlSi	—	*4.131*		*14.44*		*246.6*	[16]
$Tb_2Al_3Si_2$	$Y_2Al_3Si_2$ ($C2/m$)	10.195(2)	4.0440(7)	6.608(1)	101.169(12)	267.26	This work
$Tb_2Al_3Si_2$	—	*10.197(2)*	*4.045(1)*	*6.614(2)*	*101.11(2)*	*267.69*	[22]
$Dy_2Al_3Si_2$	$Y_2Al_3Si_2$ ($C2/m$)	10.133(3)	4.0304(9)	6.587(2)	100.73(2)	264.12	This work
$Dy_2Al_3Si_2$	—	*10.144(6)*	*4.028(3)*	*6.580(6)*	*101.04(6)*	*263.88*	[22]
$Ho_2Al_3Si_2$	$Y_2Al_3Si_2$ ($C2/m$)	10.114(2)	4.0198(5)	6.5741(10)	100.88(1)	262.48	This work
$Ho_2Al_3Si_2$	—	*10.126(1)*	*4.0266(9)*	*6.5812(8)*	*100.93(1)*	*263.48*	[21]
$Er_2Al_3Si_2$	$Y_2Al_3Si_2$ ($C2/m$)	10.0623(14)	4.0059(6)	6.5547(10)	100.697(10)	259.62	This work
$Er_2Al_3Si_2$	—	*10.083(3)*	*4.0175(9)*	*6.566(1)*	*100.73(2)*	*261.33*	[21]
$Tm_2Al_3Si_2$	$Y_2Al_3Si_2$ ($C2/m$)	10.034(4)	3.998(2)	6.536(3)	100.45(3)	257.80	This work
$Tm_2Al_3Si_2$	—	*10.043(2)*	*4.0050(8)*	*6.550(1)*	*100.54(3)*	*259.0*	[21]
$YbAl_2Si_2$	$CaAl_2Si_2$ ($P\bar{3}m1$)	4.144(2)		6.915(2)		102.9	This work
$YbAl_2Si_2$	—	*4.156(5)*		*6.914(14)*		*103.4*	[33]
LuAlSi	YAlGe ($Cmcm$)	3.9602(4)	10.049(1)	5.6071(6)		223.1	This work
LuAlSi	—	*3.9606(3)*	*10.047(1)*	*5.6099(7)*		*223.2*	[8]

Note: Data from previous studies are italicized. Cell parameters reported here were determined from powder X-ray diffraction with standard uncertainties in parentheses.

[a]Room temperature measurements unless otherwise noted.

[b]Composition determined from elemental analysis.

[c]Composition estimated from Vegard's law.

wavelength-dispersive spectrometer. The microprobe was operated at 15 nA beam current at 20 keV accelerating potential and pure elements were used as standards. Due to partial surface degradation of the rare-earth standards, somewhat broad ranges of total composition—from approximately 95–108%—were obtained. Nevertheless, the relative amounts of Al and Si were determined accurately and the resulting Al:Si ratios were found to be close to 50:50 in almost all samples. Microprobe observations agree very well with independent elemental analysis (performed on the batches from which crystals were selected for the property measurements) by Galbraith Laboratories Inc., using the ICP method. Averaging multiple measurements resulted in the following compositions (normalized per rare-earth metal): $LaAl_{1.04(3)}Si_{0.96(3)}$; $CeAl_{1.02(3)}Si_{0.98(3)}$; $PrAl_{1.19(3)}Si_{0.81(3)}$; $NdAl_{1.11(3)}Si_{0.89(3)}$; $SmAl_{1.07(3)}Si_{0.93(3)}$ and $GdAl_{0.98(3)}Si_{1.02(3)}$. The compositions of the RAl_2Si_2 (R = Eu, Yb), $R_2Al_3Si_2$ (R = Tb, Dy, Ho, Er, Tm) and LuAlSi samples were not analyzed because all other structural studies strongly suggested these are line compounds.

3. Results and discussion

3.1. Crystal structures

All compounds reported herein crystallize with well-known structure types, which shall not be discussed in further detail. Attention will be paid only to the single-crystal structure of GdAlSi, which was chosen to be a representative example of the series RAl_xSi_{2-x} (R = La, Ce, Pr, Nd, Sm, Gd).

Single-crystal X-ray diffraction data were collected for a crystal of GdAlSi in order to check and establish

the correct structure type for all RAl_xSi_{2-x} (R = La, Ce, Pr, Nd, Sm, Gd)—whether it is α-$ThSi_2$ ($I4_1/amd$) type with fully disordered Al and Si on one crystallographic site, 8*e* (Table 2), or it is an ordered ternary variant with the LaPtSi-type ($I4_1md$) in which the Al and Si would be on independent positions [23]. These considerations were prompted after the elemental analysis on single crystals of several RAl_xSi_{2-x} phases showed virtually equal Al and Si content (see Section 2). Whereas, as already mentioned, experimental results obtained on the Ce-Al-Si and Pr-Al-Si systems in particular strongly indicated the presence of wide homogeneity ranges (Fig. 1), there was little evidence that the related RAl_xSi_{2-x} (R = Sm or Gd) phases might be disordered as well. The choice of GdAlSi was also intended to verify the tetragonal symmetry derived from powder X-ray diffraction data—whereas RSi_2 or rather RSi_{2-x} binary phases, where R = La to Sm, belong to the tetragonal α-$ThSi_2$-type, the binary $GdSi_{2-x}$ crystallizes in its own α-Gd_2Si_3-type (*Imma*) [24]. The latter is simply a slight orthorhombic distortion of the tetragonal archetype, which is largely due to the decrease in atomic size of the rare-earth metals when moving across the lanthanide series. Lastly, reports on ordered ternary alumogermanides *R*AlGe with the LaPtSi ($I4_1md$) type already exist [25], and this provides further impetus for these structural studies. However, the space groups in which the α-$ThSi_2$ ($I4_1/amd$) and the LaPtSi ($I4_1md$) structures crystallize satisfy the same reflection conditions, as noted elsewhere [25]. Thus, the differentiation between the two becomes nearly impossible, especially in the case of GdAlSi, where the X-ray scattering factors of Al and Si are very similar. A trial-and-error approach was therefore applied, and structure refinements were attempted in the two space groups. The lack of convergence, the higher *R*-factors and the poorly refined anisotropic displacement parameters when the ordered LaPtSi ($I4_1md$) type was used are an indication that the α-$ThSi_2$ ($I4_1/amd$) type with fully disordered Al and Si on the 8*e* site (Table 3) is the correct structural model for GdAlSi and the related *R*AlSi (R = La, Ce, Pr, Nd, Sm) phases. Therefore, we interpret the pronounced thermodynamic stability of these nearly equiatomic ternaries as a consequence of the fact that the latter are closed-shell compounds, i.e., Zintl (valence) phases. According to the Zintl concept [26–28], because all rare-earth elements are in their trivalent state, and because each Al and Si is bonded to three Si or Al, the formula can be broken down as follows:

$$RAlSi \rightarrow 1 \times R^{3+} + 1 \times (3b - Al)^{2-} + 1 \times (3b - Si)^{1-}.$$

Similar arguments in support of the application of the Zintl concept on the related LaAlGe system have already been made [25], and were supported by EHMO band structure calculations. However, the stability of both LaAlGe and some RAl_xSi_{2-x} compounds with R = early rare-earth, extends well into the ternary phase space, as evidenced from the present and earlier experimental work [6,7,25]. This, together with the

Table 2
Selected single-crystal X-ray diffraction data collection and refinement parameters for GdAlSi

Chemical formula	GdAlSi*
Formula weight	212.32
Space group, Z	$I4_1/amd$ (No. 141), 4
Temperature	23(2) °C
Unit cell parameters	$a = 4.1255(4)$ Å
	$c = 14.432(3)$ Å
	$V = 245.63(6)$ Å^3
Radiation, λ	Mo $K\alpha$, 0.71073 Å
ρ_{calc}	5.741 g/cm^3
2θ limit	62.8°
Absorption coefficient	274.21 cm^{-1}
Collected/unique reflections	502/123 [$R_{int} = 0.0169$]
Data/restraints/parameters	123/0/8
Goodness-of-fit on F^2	1.331
Final R indices ($I > 2\sigma_{(I)}$)[a]	$R_1 = 0.0171$, w$R_2 = 0.0316$
R indices (all data)	$R_1 = 0.0260$, w$R_2 = 0.0335$
Composition from elemental analysis	$GdAl_{0.98(3)}Si_{1.02(3)}$

[a] $R_1 = \sum||F_o|-|F_c||/\sum|F_o|$; w$R_2 = [\sum[w(F_o^2-F_c^2)^2]/\sum[w(F_o^2)^2]]^{1/2}$, and $w = 1/[\sigma^2F_o^2 + (AP)^2 + BP]$, $P = (F_o^2 + 2F_c^2)/3$; A and B—weight coefficients.

Table 3
Atomic coordinates, equivalent isotropic displacement parameters (U_{ea}[a]) and important distances in Å for GdAlSi

Atom	Site	x	y		z	U_{eq} (Å^2)	Occup.
Gd	4*a*	0	3/4		1/8	0.0050(3)	1
Si	8*e*	0	1/4		0.2924(2)	0.0077(4)	0.5
Al	8*e*	0	1/4		0.2924(2)	0.0077(4)	0.5
Gd—	12 ×	Si/Al	3.1515(8)	Si/Al—		Si/Al	2.385(4)
	4 ×	Si/Al	3.176(2)		2 ×	Si/Al	2.398(2)
	4 ×	Gd	4.1255(4)		4 ×	Gd	3.1515(8)
	4 ×	Gd	4.1561(7)		2 ×	Gd	3.176(2)

[a] U_{eq} is defined as one-third of the trace of the orthogonalized U_{ij} tensor.

Table 4
Basic physical parameters of the RAl_xSi_{2-x} (α-$ThSi_2$-type; R = La-Gd), RAl_2Si_2 ($CaAl_2Si_2$-type; R = Eu, Yb) and $R_2Al_3Si_2$ ($Y_2Al_3Si_2$-type; R = Tb-Tm) compounds

Compound	Magnetic behavior	$g\sqrt{J(J+1)}$	μ_{eff} (μ_B)	θ_p (K)	T_N/T_c (K)	ρ_{298} (μΩ cm)	Reference
$LaAl_{1.04}Si_{0.96}$	Pauli paramagnetic	0	0	—	—	35	This work
$CeAl_{1.02}Si_{0.98}$	Ferromagnetic	2.54	2.28	12.3	10	68	This work
CeAlSi	*Ferromagnetic*		*2.50*	*−25.5*	*7.1*		[7]
$CeAl_{1.2}Si_{0.8}$	*Ferromagnetic*		*2.64*	*−11.0*	*<4.2*		[7]
$CeAl_{1.2}Si_{0.8}$	*Antiferromagnetic*		*2.58*	*−13.4*	*4.2*	*200*	[6]
$PrAl_{1.19}Si_{0.81}$	Ferromagnetic	3.58	3.38	25.5	17.8	60	This work
$PrAl_{1.15}Si_{0.85}$	Ferromagnetic		3.46	26.9	18.2		This work
$NdAl_{1.11}Si_{0.89}$	Antiferromagnetic	3.62	3.52	−11.4	4.8	39	This work
$SmAl_{1.07}Si_{0.93}$	Antiferromagnetic	0.85	0.65	−10	9	46	This work
$EuAl_2Si_2$	*Antiferromagnetic*	*7.94 (Eu^{2+})*	*7.82*	*23*	*35.5*	*120*	[33]
$GdAl_{0.98}Si_{1.02}$	Antiferromagnetic	7.94	7.95	−103	32	90	This work
$Tb_2Al_3Si_2$	Antiferromagnetic	9.72	9.24	−26.8	15.8	22	This work
$Dy_2Al_3Si_2$	Antiferromagnetic	10.65	10.66	−17.8	11.8	29	This work
$Ho_2Al_3Si_2$	Antiferromagnetic	10.61	10.4	−15.2	7.8 and 4.5	17	This work
$Ho_2Al_3Si_2$	*Antiferromagnetic*		*11.2*	*−10.5*	*7*	*~25*	[21]
$Er_2Al_3Si_2$	Antiferromagnetic	9.58	9.68	−6.1	4.2	19	This work
$Er_2Al_3Si_2$	*Antiferromagnetic*				*<4*	*~25*	[21]
$Tm_2Al_3Si_2$	Antiferromagnetic	7.56	7.64	6.4	8.6 and 2.9	190	This work
$Tm_2Al_3Si_2$	*Antiferromagnetic*		*7.58*	*4*	*7*	*~25*	[21]
$YbAl_2Si_2$	Pauli paramagnetic	0 (Yb^{2+})	0				This work
$YbAl_2Si_2$	*mixed-valent Yb^{2+}/Yb^{3+}*	*4.54 (Yb^{3+})*	*2.57*	*−382*			[29]
LuAlSi	Pauli paramagnetic	0	0				This work

Note: Results from previous studies, where available, are shown in *italics*.

observed metallic properties (Table 4), may suggest that the above-mentioned formal electron count is overly simplistic, as fixed stoichiometry and semiconducting behavior are characteristics of the classic Zintl phases. Our recent structural and computational studies on the metallic behavior in another Zintl phase, $EuGe_2$ [29], demonstrate that the classic Zintl reasoning, ignoring the contributions between cations and polyanions oversimplifies this simple rare-earth-based germanide as being a semiconducting material. In that sense, the equiatomic *R*AlSi and *R*AlGe ternaries can be regarded as *metallic* Zintl phases, which are capable of forming thermodynamically stable solid solutions RAl_xSi_{2-x} and RAl_xGe_{2-x}. Therefore, it will be important to study in deeper detail the properties of more solid solution phases across the regions of structural stability, especially for the early members of the lanthanide family. For these *f*-block elements, the larger size of the R^{3+} cations may provide for some unrecognized but important *R*–*R* interactions, which could explain the great variation of physical properties by simply alloying the polyanionic Si-based framework with electron poorer Al. This process not only changes the number of valence electrons but also expands the lattice as the covalent radius for Al is nearly 7% larger than that of Si [30]. This, in turn, results in significant lattice expansion/contractions, especially along the *c*-direction—e.g., there is a difference of almost 1.1 Å going from $CeSi_{2-x}$ with $c = 13.815$ Å to $CeAl_{1.4}Si_{0.6}$ with $c = 14.90$ Å (Table 1). Since both the bond distances and the electron count vary simultaneously, the subsequent crystal structure and property investigations should be coupled with comprehensive band structures analyses to fully elucidate the nature of these phenomena.

3.2. Phase equilibria

Several comprehensive studies have dealt with the phase equilibria in certain isothermal sections of the *R*-Al-Si phase diagrams [1,2,6–9]. Tremendous efforts have been made to identify and structurally characterize all structure types in which the binary *R*-Si, *R*-Al, and the corresponding *R*-Al-Si phases crystallize.

In the Si-rich part of the phase diagrams [31], there are three major types in which the corresponding binary compounds crystallize: (1) α-$ThSi_2$ ($I4_1/amd$); (2) α-Gd_2Si_3 (*Imma*); and (3) AlB_2 ($P6/mmm$). The structure types observed depend largely on the atomic radius of the rare-earth and the degree of non-stoichiometry (most of these are non-stoichiometric phases as already discussed). Thus, the early lanthanide RSi_{2-x} compounds (R = La-Sm, i.e., larger cations) predominantly crystallize in the α-$ThSi_2$-type. Moving to the right in the rare-earth series, i.e., decreasing atomic size, gradual transitions to orthorhombically distorted α-Gd_2Si_3-type, and hexagonal AlB_2 are observed. In many

non-stoichiometric RSi_{2-x} compounds, especially with the late lanthanides, partial ordering of the vacancies frequently results in novel structure types and superstructures [1–3].

Similar systematic evolutions can be inferred for the binary *R*-Al compounds [3], but insights are more difficult in the ternary *R*-Al-Si systems, because there are more than 10 common structure types in which these materials crystallize [1–3]. Effects such as ternary solid solubility and the existence of low and high-temperature modifications complicate the structural analysis even further. Some classifications and systematic studies of equiatomic *R*AlSi [8] and *R*AlGe [8,12,32] have already been published. These structural data on "on-stoichiometry" prepared compounds establish that when *R* is a small rare-earth (Tb-Lu), the corresponding *R*AlSi and *R*AlGe compounds crystallize with the orthorhombic YAlGe-type [8,12]. In contrast, when *R* is a large rare-earth (La-Gd), the tetragonal α-$ThSi_2$-type (or its ordered variant) is realized. Exploration of the nearly equiatomic *R*-Al-Si, *R*-Al-Ge and *R*-Al-Sn sections of the corresponding phase diagrams (R = La to Gd), done by means of arc-melting and subsequent annealing, suggests that the structure types in which the resulting ternary compounds crystallize strongly depend on the valence electron concentrations [16]. Our studies carried out with fixed *R*:Si ratios (~1:2) under Al flux-growth conditions (i.e., large excess of Al), show that certain crystal structure types appear dominant for specific lanthanides. These can be divided in two large subgroups in regard to the rare-earth size: the first half of the trivalent rare-earth metals (R = La-Gd) invariably yields RAl_xSi_{2-x} with the α-$ThSi_2$ structure, whereas the second half favors the formation of $R_2Al_3Si_2$ with the $Y_2Al_3Si_2$ structure (R = Tb-Lu). The last lanthanide element, Lu, under the same conditions forms LuAlSi with the YAlGe-type, a deviation from the general trends which is most certainly due to very small ionic size and/or completely filled *f*-shell. Eu and Yb are certainly exceptions from the two subgroups due to their tendency to be in divalent oxidation states, a result of the stabilization of half-filled and completely filled *f*-shells for Eu^{2+} and Yb^{2+}, respectively. Thus, independent of the differences in the Eu^{2+} and Yb^{2+} ionic radii, the corresponding Eu-Al-Si and Yb-Al-Si reactions at these specific conditions (above) yield RAl_2Si_2 (R = Eu, Yb) with the trigonal $CaAl_2Si_2$-type [33].

It is interesting to note that in all of our studies, initial *R*:Si:Al ratios were always kept close to 1:2:20, yet a ratio of *R*:Si = 1:2 in the reaction products is preserved only in the case of RAl_2Si_2 (R = Eu, Yb). These two flux reactions prove to be particularly sensitive to this stoichiometric ratio, and by employing Si-leaner conditions, crystals of $EuAl_xSi_{2-x}$ (AlB_2-type) or even $EuAl_xSi_{4-x}$ ($BaAl_4$-type), and YbAlSi (YAlGe-type) can be grown successfully from Al flux using variations of the temperature profiles described above [34]. Experimental efforts to precisely determine the phase boundaries in these systems are currently underway.

On the other hand, all other reactions loaded with compositions *R*:Si:Al = 1:2:20 (R = rare-earth, excluding Eu, Yb) afford the formation of *R*AlSi and $R_2Al_3Si_2$, where the *R*:Si ratio in the products is exactly or close to 1:1. This may indicate that at temperatures above 700 °C, in that section of ternary phase space, *R*AlSi (or rather $RAl_{1-x}Si_{1+x}$) and $R_2Al_3Si_2$ are the most thermodynamically stable phases. Our exploratory studies demonstrate that small changes in the initial composition do not affect the reaction outcome in these cases, whereas small changes in the heat treatment apparently shift the phase equilibria in the RAl_xSi_{2-x} solid solutions, as seen, e.g., in the Ce-Al-Si system (Fig. 1). The stoichiometric breadth of these RAl_xSi_{2-x} ternaries is strongly dependent on the nature of *R*, with x varying between ~0.4 and ~1.4 in the case of La, Ce or Pr [6,7,9,16]. For $SmAl_xSi_{2-x}$ and $GdAl_xSi_{2-x}$ (i.e., those with considerably smaller ionic radii), the phase width appears to be much narrower with x in the range of ~0.9 to ~1.1.

Nearly equiatomic RAl_xSi_{2-x} (R = La, Ce, Pr, Nd, Sm, Gd) phases, i.e., x~1, can be made in a rational manner from pure elements in high yields, whereas reactions intended to produce $R_2Al_3Si_2$ (R = Tb, Dy, Ho, Er, Tm) from stoichiometric pure elements yield mixtures of phases. This seems to indicate that RAl_xSi_{2-x} with the α-$ThSi_2$ structure are the most thermodynamically stable phases at all temperatures for nearly equiatomic compositions in all *R*-Al-Si (R = La, Ce, Pr, Nd, Sm, Gd) systems, and the structural stability is governed by a delicate interplay of electronic and packing requirements as discussed above. In contrast, the $R_2Al_3Si_2$ (R = Tb, Dy, Ho, Er, Tm) compounds are apparently high-temperature phases and their stability is probably determined by the packing requirements of the rare-earth metals. In the case of RAl_2Si_2 (R = Eu, Yb), both can be made in high yields from reactions loaded "on-stoichiometry", which suggests that these are thermodynamically stable phases in the Eu-Al-Si and Yb-Al-Si systems at these compositions and temperatures. Additionally, the fact that this structure type is adopted only by the divalent cations indicates that electronic requirements play a crucial role in structure stability. Comprehensive band calculations on the $CaAl_2Si_2$-type can be found elsewhere [35].

3.3. Physical properties

Details on the electronic and magnetic properties of each *R*-Al-Si compound described in the previous section will be given full consideration elsewhere. Herein, we present a brief comparative description of the basic features of the title compounds, as well as

highlight some peculiarities in the evolution of physical properties. Important physical parameters are summarized in Table 4.

3.4. $CeAl_xSi_{2-x}$

There are a few reports on the properties of $CeAl_xSi_{2-x}$ with the α-$ThSi_2$-type and they do not agree [6,7,9]. Aside from the fact that $CeAl_xSi_{2-x}$ exists as an almost infinite number of solid solution phases, there are large variations between the properties of Ce-Al-Si samples with apparently identical compositions [6,7,9]. For instance, the Al-rich phase $CeAl_{1.2}Si_{0.8}$ is reported by Dhar and Pattalwar [7] to order ferromagnetically below 4.2 K, while another group reports antiferromagnetic behavior for a sample with the same composition [6]. Both of these studies were performed with polycrystalline samples, which may explain this variation. Our single-crystal study provides further evidence for ferromagnetic order in $CeAl_xSi_{2-x}$ with $0.8<x<1$, as can be seen in Fig. 2, which supports the results of Jung et al. [9], also obtained on flux-grown crystals. The observed effective moment deviates somewhat from that expected free ion Ce^{3+} moment of 2.54 μ_B, most likely due to the strong anisotropy in $\chi(T)$ for $H||c$ and $H\perp c$. Additionally, the observed curvature in $\chi^{-1}(T)$ suggests that these materials exhibit strong crystal field interactions below about 100 K (Fig. 2, inset). Field-dependent magnetization measurements at 5 K for $CeAl_{1.02}Si_{0.98}$ reveal a tendency for saturation at sufficiently high magnetic fields ($\sigma\sim0.92\,\mu_B$ at 50 kG). Resistivity data taken on $CeAl_{1.02}Si_{0.98}$ crystals confirm the magnetic ordering temperature derived from the magnetic measurements, as evidenced from the kink in the $\rho(T)$ curvature at around 10 K (Fig. 3, inset). The relatively high room temperature resistivity (Fig. 3), and the small resistivity ratio (on the order of 4) indicate that $CeAl_{1.02}Si_{0.98}$ may be a poor metal. These observations and the ferromagnetic ground states are further corroborated by calorimetry and Hall-coefficient measurements that reveal a low carrier density [36]. Thus, all of the above seems consistent with charge-balancing arguments, e.g., $(Ce^{3+})(3b\text{-}Al^{2-})(3b\text{-}Si^{1-})$ based on the Zintl formalism (see Section 3.1).

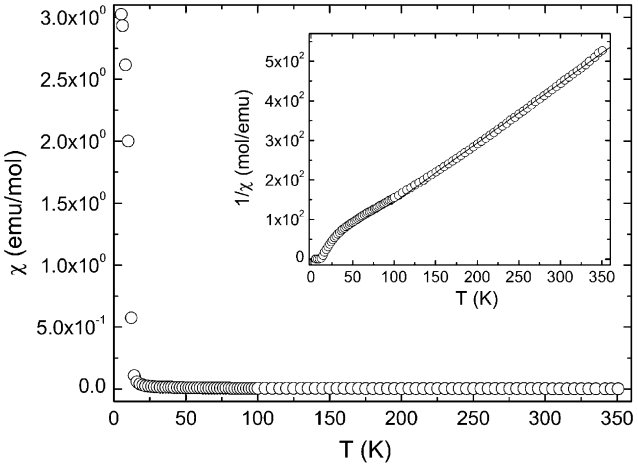

Fig. 2. Magnetic susceptibility $\chi(T)$ for a single crystal ($H||c$) of $CeAl_{1.02}Si_{0.98}$, measured in a magnetic field $H = 1$ kG. Inset: Inverse magnetic susceptibility $\chi^{-1}(T)$. The departures from linear $\chi^{-1}(T)$ Curie–Weiss behavior are likely due to thermal population of excited crystal field levels and ferromagnetic interactions.

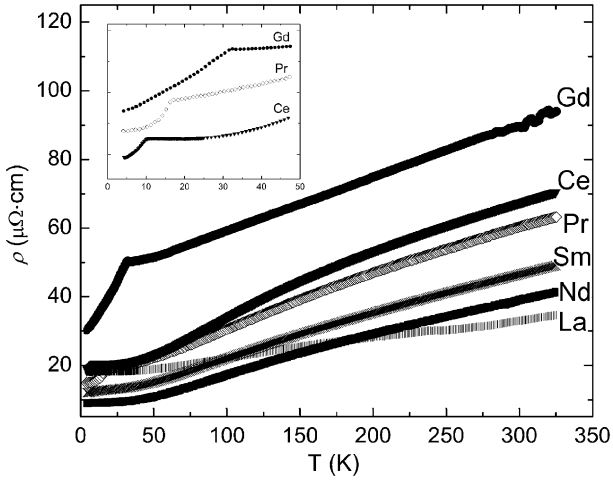

Fig. 3. Four-probe electrical resistivity data for all RAl_xSi_{2-x} phases (R = La, Ce, Pr, Nd, Sm, Gd) crystallizing with the α-$ThSi_2$-type. Inset: Resistivity (arbitrary units) for $CeAl_xSi_{2-x}$, $PrAl_xSi_{2-x}$ and $GdAl_xSi_{2-x}$ at temperatures near their respective magnetic transitions.

3.5. $PrAl_xSi_{2-x}$

Similar to $CeAl_xSi_{2-x}$, a wide homogeneity range also exists for $PrAl_xSi_{2-x}$. Hence, magnetization measurements were performed on a crystal with composition $PrAl_{1.19}Si_{0.81}$, i.e., with $x\sim0.2$, a value determined from elemental analysis (Table 1), as well as for a crystal with composition close to $PrAl_{1.15}Si_{0.85}$ (inferred from the difference in the unit cell constants; $a = 4.2263(1)$ Å; $c = 14.5343(5)$ Å; $V = 259.61$ Å^3 for $PrAl_{1.19}Si_{0.81}$, and $a = 4.2245(1)$ Å; $c = 14.4731(5)$ Å; $V = 258.29$ Å^3 for $PrAl_{1.15}Si_{0.85}$, respectively). Both samples were found to order ferromagnetically below $T_c\sim18$ K (Fig. 4a). The effective moments determined from fitting the data above 50 K with the Curie–Weiss law are very close to that expected for Pr^{3+} (Table 4). Heat capacity data taken on a crystal of $PrAl_{1.19}Si_{0.81}$ confirm the ordering temperature derived from the $\chi(T)$ dependence. Electrical resistivity measurements on both samples exhibit a small drop in $\rho(T)$ at $T = 18\,K$, corresponding to the onset of ferromagnetic order (Fig. 3, inset). The room temperature resistivity $\rho_{298}\sim60\,\mu\Omega$ cm is higher than that

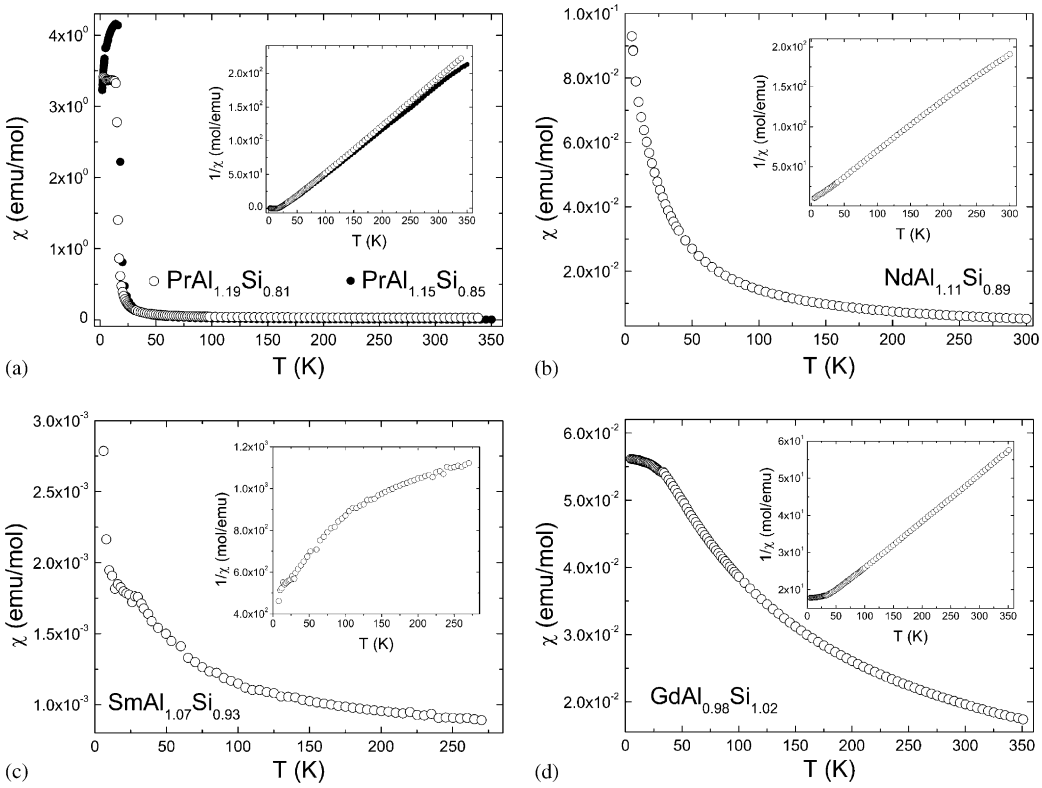

Fig. 4. Magnetic susceptibility $\chi(T)$ for $PrAl_xSi_{2-x}$ (a), $NdAl_xSi_{2-x}$ (b), $SmAl_xSi_{2-x}$ (c) and $GdAl_xSi_{2-x}$ (d), measured on single crystals in a magnetic field $H = 1$ kG with $H||c$. Inset: Inverse magnetic susceptibility $\chi^{-1}(T)$. For $PrAl_xSi_{2-x}$ (a), two measurements on samples with slightly different compositions are superimposed; variation in their respective behavior is observed.

expected for a normal metal, which together with the small residual resistivity ratio and the high residual resistivity $\rho_0 \sim 15\,\mu\Omega$ cm provides further evidence in support of the above-mentioned Zintl concept. More comprehensive property measurements on a greater variety of $PrAl_xSi_{2-x}$ phases are currently under way.

3.6. $NdAl_xSi_{2-x}$

Measurements are reported for a phase with composition $NdAl_{1.11(3)}Si_{0.89(3)}$. This compound, unlike its Ce- and Pr-counterparts, orders antiferromagnetically at $T_N \sim 4.8$ K, determined from the mid-point of the jump in $d\chi/dT$ (Fig. 4b). An anomaly in the specific heat $C(T)$ data at the same temperature confirms long-range order. Above the Néel temperature, $\chi(T)$ behavior follows the Curie–Weiss law, and fitting the linear $1/\chi(T)$ data yields an effective moment $\mu_{eff} = 3.52\,\mu_B$, close to that expected for Nd^{3+} ($\mu_{eff} = 3.62\,\mu_B$), and a Weiss constant $\theta_p = -11.4$ K. Resistivity measurements show $NdAl_{1.11(3)}Si_{0.89(3)}$ to be metallic (Fig. 3), with room temperature resistivity $\rho_{298} \sim 40\,\mu\Omega$ cm (Table 4), and residual resistivity $\rho_0 \sim 9\,\mu\Omega$ cm. Since the antiferromagnetic ordering temperature is below 5 K and the measurements were carried out only down to that temperature, no anomalies in $\rho(T)$ are observed.

3.7. $SmAl_xSi_{2-x}$

Magnetization measurements were performed for only one sample with composition $SmAl_{1.07(3)}Si_{0.93(3)}$. Because of the small effective moment on Sm^{3+} (Table 4) and the significant diamagnetic core and strong van Vleck paramagnetic contributions to the magnetization, the data were fitted with the modified Curie–Weiss law $\chi(T) = \chi_0 + C/(T-\theta_p)$ [37], which resulted in $\chi_0 = 7.4 \times 10^{-5}$ emu/mol and $\theta_p = -10$ K (Fig. 4c). The calculated effective moment $\mu_{eff} = 0.65\,\mu_B$ is close to that expected for Sm^{3+} (Table 4). Field-dependent measurements at 2, 5 and 10 K for the same sample do not show a tendency for saturation up to magnetic of 50 kG. Reliable determination of the ordering temperature from the susceptibility data was not possible, but specific heat measurements in the range 2–20 K reveal two anomalies at approximately 9.5 and 5.5 K. These are likely indications of antiferromagnetic order; however, more measurements on different samples are needed to confirm this. Resistivity data taken on single crystals of $SmAl_{1.07(3)}Si_{0.93(3)}$ reveal metallic behavior (Fig. 3), with $\rho_{298} \sim 46\,\mu\Omega$ cm and $\rho_0 \sim 12\,\mu\Omega$ cm, respectively. To determine the carrier concentrations and the nature of the relatively better conductivities for both $NdAl_{1.11(3)}Si_{0.89(3)}$ and $SmAl_{1.07(3)}Si_{0.93(3)}$, Hall-coefficient measurements are presently in progress.

3.8. $GdAl_xSi_{2-x}$

A crystal of $GdAl_{0.98(3)}Si_{1.02(3)}$ was thoroughly characterized by means of single-crystal X-ray diffraction (above), magnetic and resistivity measurements. Similar to all other *R*-Al-Si phases discussed herein with the α-$ThSi_2$ ($I4_1/amd$) type, GdAlSi is a poor metal with room temperature resistivity $\rho_{298}\sim 90\,\mu\Omega\,cm$ (Table 4), and residual resistivity $\rho_0\sim 30\,\mu\Omega\,cm$. A kink in $\rho(T)$ is found at ~32 K (Fig. 3, inset), corresponding to the onset of antiferromagnetic order, an observation that was confirmed from the analysis of the magnetic susceptibility data (Fig. 4d). Above the Néel temperature $T_N = 32\,K$, $\chi(T)$ follows the Curie–Weiss law, yielding an effective moment $\mu_{eff} = 7.95\,\mu_B$, close to that expected for Gd^{3+} ($\mu_{eff} = 7.94\,\mu_B$), and a Weiss constant $\theta_p = -103\,K$. Jung et al. [9] report on very similar bulk magnetism data, also obtained on flux-grown crystals, although their work suggests slightly different composition—$GdAl_{0.9}Si_{1.1}$.

3.9. $R_2Al_3Si_2$ (R = Tb-Tm)

Reports on the crystal structures and some of the properties of these compounds exist [21,22]. These materials crystallize as long needle-shaped crystals and all magnetic measurements were performed with magnetic field parallel to the direction of the needle, which was assumed to be the *b*-axis. Because of the low symmetry, monoclinic, the orientation of the *a*- and *c*-axis within the plane perpendicular to the magnetic field remained unknown. Multiple measurements on the same crystals in different orientations (the external magnetic field always parallel to the needle-axis) revealed very strong magnetic anisotropy, as expected for such a low crystal symmetry. The magnetic susceptibility vs. temperature for $R_2Al_3Si_2$ (R = Tb-Er) is shown in Fig. 5. Cusp-like features are visible in the data at ~16, ~12, ~8 and ~4 K for $Tb_2Al_3Si_2$, $Dy_2Al_3Si_2$, $Ho_2Al_3Si_2$ and $Er_2Al_3Si_2$, respectively, indicating the onset of long-range antiferromagnetic order in these materials. Careful measurements on $Ho_2Al_3Si_2$ show that this compound undergoes another transition at ~4.5 K. The corresponding Néel temperatures (T_N) were determined from the mid-point of the jump in $d\chi/dT$ and are given in Table 4. Above the Néel temperatures, $\chi(T)$ for all four follow the Curie–Weiss law, and fitting the inverse susceptibility data to a linear equation gives the effective moment $\mu_{eff} = 9.24\,\mu_B$ for Tb^{3+} in $Tb_2Al_3Si_2$, $\mu_{eff} = 10.66\,\mu_B$ for Dy^{3+} in

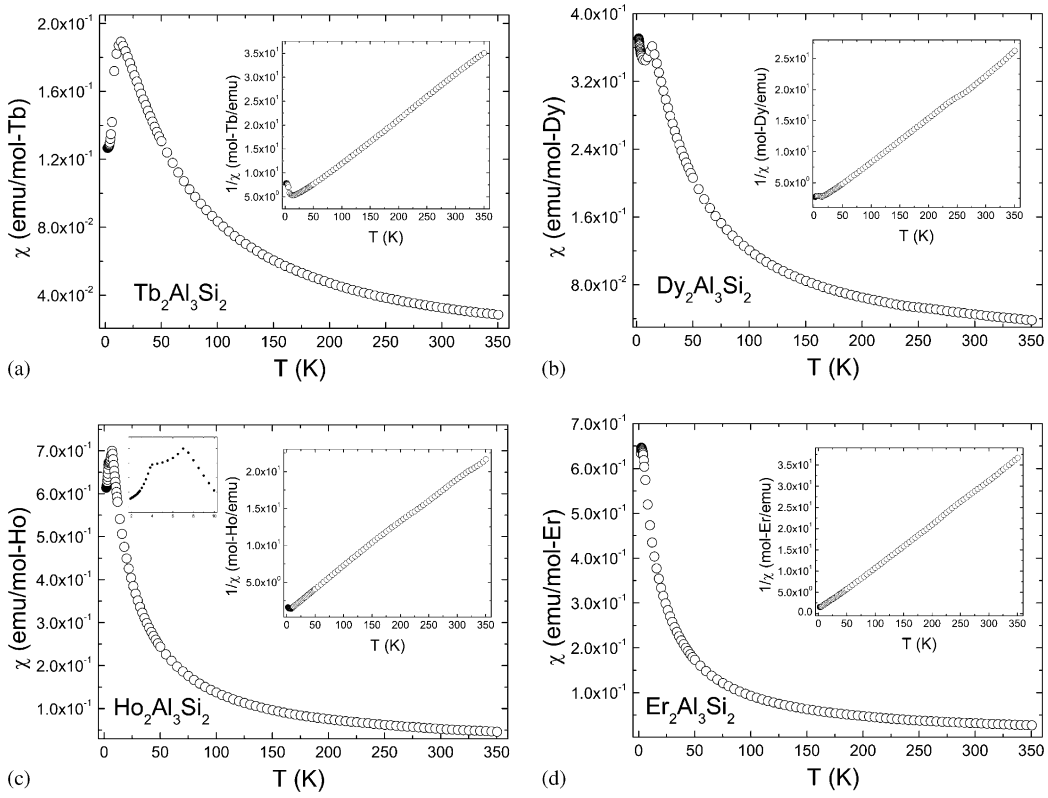

Fig. 5. Magnetic susceptibility $\chi(T)$ for $Tb_2Al_3Si_2$ (a), $Dy_2Al_3Si_2$ (b), $Ho_2Al_3Si_2$ (c) and $Ho_2Al_3Si_2$ (d), measured on single crystals in a magnetic field $H = 1\,kG$ with $H||b$. Inset: Inverse magnetic susceptibility $\chi^{-1}(T)$. For $Ho_2Al_3Si_2$ (c), the upper left inset shows the presence of two transitions at around 7.8 and 4.5 K, respectively.

$Dy_2Al_3Si_2$, $\mu_{eff} = 10.4\,\mu_B$ for Ho^{3+} in $Ho_2Al_3Si_2$, $\mu_{eff} = 9.68\,\mu_B$ for Er^{3+} in $Er_2Al_3Si_2$, respectively. The derived negative Weiss constants range from $\theta_p = -26.8$ to –6.1 K, indicating weak antiferromagnetic interactions. These numbers compare well with the theoretical values for free ions (Table 4), although some discrepancies exist between these values and that which is reported in the literature [21]. Most likely, these disagreements are due to strong magnetic anisotropy and differences in the measuring techniques, e.g., oriented single crystals vs. powdered polycrystalline samples. The ordering temperatures derived from the magnetic susceptibility data are corroborated with resistivity measurements (Fig. 6), which show all $R_2Al_3Si_2$ (R = Tb, Dy, Ho, Er) phases to be good metals with room temperature resistivities $\rho_{298} \sim 20-25\,\mu\Omega\,cm$, and very low residual resistivities $\rho_0 \sim 2-5\,\mu\Omega\,cm$. In the case of $Tm_2Al_3Si_2$, the room temperature resistivity $\rho_{298} \sim 190\,\mu\Omega\,cm$, and the residual resistivity $\rho_0 \sim 15\,\mu\Omega\,cm$ are considerably higher (below).

The results from the magnetic measurements obtained for $R_2Al_3Si_2$ (R = Tb, Dy, Ho, Er) are in good agreement with those expected from the de Gennes scale [38], as evidenced from Fig. 7. However, data for $Tm_2Al_3Si_2$ evidently deviate from it, as the first antiferromagnetic ordering that $Tm_2Al_3Si_2$ undergoes is at temperature $T_N = 8.6$ K. The experimental Néel temperature value, determined from the mid-point of the jump in $d\chi/dT$, is almost three times higher than what the theory predicts. Additionally, the compound undergoes a second transition at around 2.9 K (Fig. 8, left inset), which coincides with the expected T_N from de Gennes scale [38]. Four-probe resistivity measurements provide additional evidence for both transitions, as shown in Fig. 9. Above the Néel temperatures, the magnetization data obey the Curie–Weiss law and an effective moment of 7.56 μ_B (Table 4) can be easily

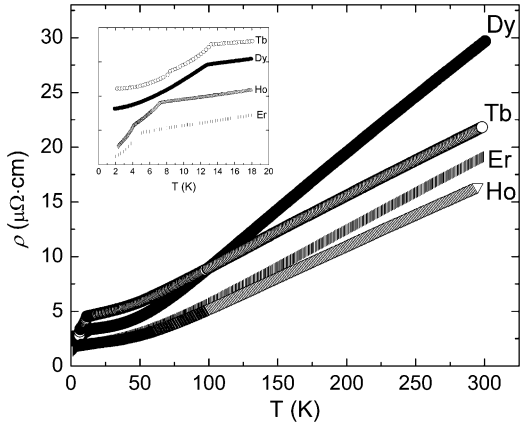

Fig. 6. Four-probe electrical resistivity for $R_2Al_3Si_2$ phases (R = Tb, Dy, Ho, Er), crystallizing with the C-centered monoclinic $Y_2Al_3Si_2$-type. Inset: Resistivity (arbitrary units) at temperatures near the respective antiferromagnetic transitions.

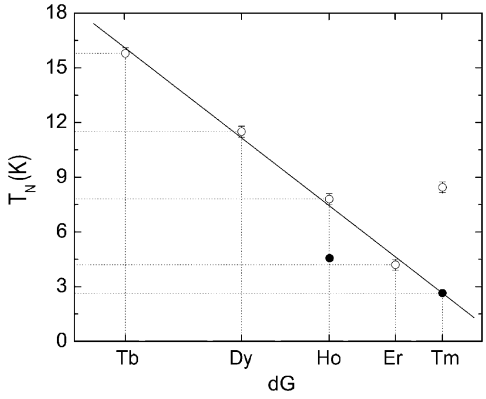

Fig. 7. Néel temperatures (T_N) for all $R_2Al_3Si_2$ phases (R = Tb, Dy, Ho, Er, Tm) plotted vs. the de Gennes [38] factors for Tb, Dy, Ho, Er and Tm, respectively. First transition temperatures are shown with open circles, the second transition temperatures for $Ho_2Al_3Si_2$ and $Tm_2Al_3Si_2$ are drawn in black circles. A departure from the almost linear scale is clearly seen for the Tm-analog.

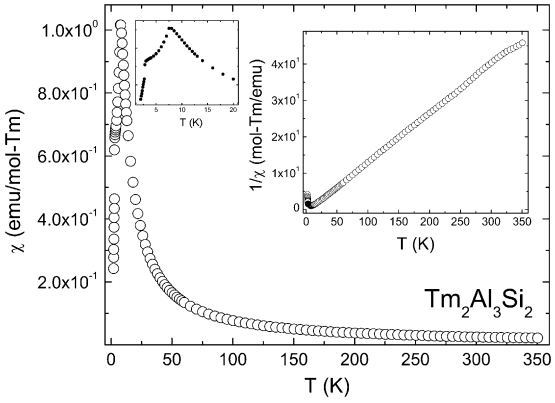

Fig. 8. Magnetic susceptibility $\chi(T)$ for $Tm_2Al_3Si_2$, measured on a single crystal in a magnetic field $H = 1$ kG with $H||b$. Right inset: Inverse magnetic susceptibility $\chi^{-1}(T)$. Upper left inset: Magnified view of the magnetic susceptibility $\chi(T)$ plot around the two transitions at 8.6 and 2.9 K, respectively.

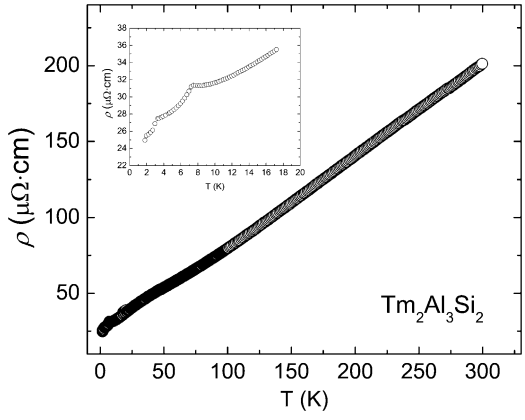

Fig. 9. Four-probe electrical resistivity for $Tm_2Al_3Si_2$. Inset: Resistivity at temperatures near the respective antiferromagnetic transitions.

obtained. This effective moment and Weiss constant $\theta_p = 6.4\,K$ compare well with the theoretical μ_{eff} for Tm^{3+} ion, as well as with previously reported data on $Tm_2Al_3Si_2$ [21]. The ordering temperatures between the present and the earlier study agree fairly well, although the latter work on polycrystalline sample provides no evidence for the existence of second antiferromagnetic transition at 2.9 K. It rather discusses the possibility for a metamagnetic transition at a critical field of about 6 kG.

3.10. $YbAl_2Si_2$ and $EuAl_2Si_2$

The structures and the properties of these two materials have been fully characterized in an earlier publication by Kranenberg et al. [33,39]. The results reported therein have been obtained on polycrystalline samples, and our measurements on single crystals reproduce most of the data within the experimental errors. A noteworthy difference between the two studies is the magnetism of $YbAl_2Si_2$, which has been interpreted originally as a mixed-valent compound [33], whereas our experimental results on single crystals fail to provide any evidence for mixed-valency. For that matter, discrepancies between the measurements on the same compounds in polycrystalline and single-crystal forms are not unprecedented [40,41]. This is especially true for Ce-, Eu- and Yb-based intermetallics, where interplay between oxidation states is possible, and traces of unrecognized impurities in polycrystalline samples may lead to errors in the experimental data and inaccurate interpretations. Systematic magnetic, resistivity and calorimetry measurements on single crystals $EuAl_2Si_2$ and $YbAl_2Si_2$ will be reported in a forthcoming publication [13].

4. Conclusions

Reactions of all *R* (rare-earth) with Si and Al have been explored. Using Al in 20-fold excess as a flux, large single crystals of several types of ternary *R*-Al-Si phases were obtained. Depending on the nature (size) of *R*, the outcome of these flux reactions can be systematized as follows: (1) the early trivalent rare-earths (R = La, Ce, Pr, Nd, Sm, Gd) yield solid solution RAl_xSi_{2-x} phases, which are ternary derivatives of the body-centered tetragonal α-$ThSi_2$-type; (2) the late trivalent rare-earths (R = Tb, Dy, Ho, Er, Tm) form stoichiometric $R_2Al_3Si_2$ compounds which crystallize in the *C*-centered monoclinic $Y_2Al_3Si_2$-type; (3) the divalent Eu and Yb behave differently, as expected, and produce $EuAl_2Si_2$ and $YbAl_2Si_2$ with the trigonal $CaAl_2Si_2$-type, while the last lanthanide element, Lu, forms LuAlSi with the *C*-centered orthorhombic YAlGe-type.

Acknowledgments

Svilen Bobev acknowledges financial support from the University of Delaware (through start-up funds), the Los Alamos National Laboratory Directed Research and Development program (LANL/LDRD), and the Institute for Complex Adaptive Matter (I.C.A.M.). Work at LANL was performed under the auspices of the US Department of Energy.

References

[1] A. Iandelli, A. Palenzona, Crystal chemistry of intermetallic compounds, in: K.A. Gschneidner Jr, L. Eyring (Eds.), Handbook on the Physics and Chemistry of Rare Earths, vol. 2, North-Holland, Amsterdam, 1979, p. 1.
[2] A. Szytula, J. Leciejewicz (Eds.), Handbook of Crystal Structures and Magnetic Properties of Rare Earth Intermetallics, CRC Press, Boca Raton, FL, 1994.
[3] P. Villars, L.D. Calvert (Eds.), Pearson's Handbook of Crystallographic Data for Intermetallic Compounds, second ed., American Society for Metals, Materials Park, OH, 1991 and the desktop edition, 1997.
[4] M. Kohgi, M. Ito, T. Satoh, H. Asano, T. Ishigaki, F. Izumi, J. Magn. Magn. Mater. 90 (1990) 433.
[5] P.C. Canfield, Z. Fisk, Philos. Mag. B 65 (1992) 1117.
[6] H. Flandorfer, D. Kaczorowski, J. Gröbner, P. Rogl, R. Wouters, C. Godart, A. Kostikas, J. Solid State Chem. 137 (1998) 191.
[7] S.K. Dhar, S.M. Pattalwar, J. Magn. Magn. Mater. 152 (1996) 22.
[8] S. Pukas, Y. Lutsyshyn, M. Manyako, E. Gladyshevskii, J. Alloys Compounds 367 (2004) 162.
[9] M.H. Jung, S.H. Park, H.C. Kim, Y.S. Kwon, arXiv:cond-mat/0304235.
[10] T.I. Yanson, M.B. Manyako, O.I. Bodak, R.E. Gladyshevskii, R. Cerny, K. Yvon, Acta Cryst. C 50 (1994) 1377.
[11] E.I. Gladyshevskii, P.I. Kripyakevich, O.I. Bodak, Ukr. Fiz. Zh. 12 (1967) 447.
[12] J.T. Zhao, E. Parthé, Acta Cryst. C 38 (1990) 2276.
[13] [a] S. Bobev, P. Tobash, unpublished.
[b] S. Bobev, V. Fritsch, J.D. Thompson, J.L. Sarrao, in preparation.
[14] JADE Version 6.5, Materials Data Inc., Livermore, CA, 2003.
[15] A.C. Larson, R.B. von Dreele, GSAS-General Structure Analysis System; LAUR 86-748, Los Alamos National Laboratory, Los Alamos, NM, 1986.
[16] A. Raman, H. Steinfink, Inorg. Chem. 6 (1967) 1789.
[17] SMART NT Version 5.05, Bruker Analytical X-ray Systems Inc., Madison, WI, 1998
[18] SAINT NT Version 6.22, Bruker Analytical X-ray Systems Inc., Madison, WI, 2001.
[19] SADABS NT Version 2.05, Bruker Analytical X-ray Systems Inc., Madison, WI, 1998.
[20] SHELXTL Version 5.10, Bruker Analytical X-ray Systems Inc., Madison, WI, 1997.
[21] C. Kranenberg, A. Mewis, Z. Anorg. Allg. Chem. 626 (2000) 1448.
[22] X.Z. Chen, B. Sieve, R. Henning, A.J. Schultz, P. Brazis, C.R. Kannerwurf, J.A. Cowen, R. Crosby, M.G. Kanatzidis, Angew. Chem. Int. Ed. 38 (1999) 693.
[23] K. Klepp, E. Parthé, Acta Cryst. B 38 (1982) 1105.
[24] J.A. Perri, I. Binder, B. Post, J. Phys. Chem. 63 (1959) 616.
[25] A.M. Guloy, J.D. Corbett, Inorg. Chem. 30 (1991) 4789.
[26] E. Zintl, Angew. Chem. 52 (1939) 1.
[27] H.-G. von Schnering, Angew. Chem. Int. Ed. Engl. 20 (1981) 33.

[28] S.M. Kauzlarich (Ed.), Chemistry, Structure and Bonding of Zintl Phases and Ions, VCH Publishers, New York, 1996 and the references therein.
[29] S. Bobev, E.D. Bauer, J.D. Thompson, J.L. Sarrao, G.J. Miller, B. Eck, R. Dronskowski, J. Solid State Chem. 177 (2004) 3545.
[30] L. Pauling, The Nature of the Chemical Bond, third ed., Cornell University Press, Ithaca, NY, 1960.
[31] T.B. Massalski, in: Binary Alloy Phase Diagrams, American Society for Metals, Materials Park, OH, 1990.
[32] E.I. Gladyshevskii, N.Z. Nakonechna, K. Cenzual, R.E. Gladyshevskii, J.L. Jorda, J. Alloys Compounds 296 (2000) 265.
[33] C. Kranenberg, D. Johrendt, A. Mewis, R. Pöttgen, G. Kotzyba, C. Rosenhahn, B.D. Mosel, Solid State Sci. 2 (2000) 215.
[34] P. Tobash, S. Bobev, unpublished.
[35] C. Zheng, R. Hoffmann, R. Nesper, H.-G. von Schnering, J. Am. Chem. Soc. 108 (1986) 1876.
[36] S. Bobev, J.D. Thompson, Z. Fisk, M.F. Hundley, J.L. Sarrao, unpublished.
[37] J.S. Smart, Effective Field Theories of Magnetism, Saunders, Philadelphia, PA, 1966.
[38] P.G. de Gennes, J. Phys. Radium 23 (1962) 510.
[39] C. Kranenberg, D. Johrendt, A. Mewis, Z. Anorg. Allg. Chem. 625 (1999) 1787.
[40] P.G. Pagliuso, J.L. Sarrao, J.D. Thompson, M.F. Hundley, M.S. Sercheli, R.R. Urbano, C. Rettori, Z. Fisk, S.B. Oseroff, Phys. Rev. B 63 (2001) 092406.
[41] J.C.P. Klaasse, F.R. de Boer, P.F. de Châtel, Physica B 106 (1981) 178.